Temperature-Induced Conformational Transition of Intestinal Fatty Acid Binding Protein Enhancing Ligand Binding: A Functional, Spectroscopic, and Molecular Modeling Study†

Cecilia N. Arighi, Juan Pablo F. C. Rossi, and José M. Delfino*

Department of Biological Chemistry and Institute of Biochemistry and Biophysics (IQUIFIB), School of Pharmacy and Biochemistry, University of Buenos Aires, Junín 956, 1113 Buenos Aires, Argentina

Received July 29, 1998; Revised Manuscript Received September 18, 1998

ABSTRACT: Intestinal fatty acid binding protein (IFABP) undergoes a reversible thermal transition between 35 and 50 °C, as revealed by circular dichroism spectroscopy in the near-UV region. For the apoprotein, the molar ellipticity measured at 254 nm (possibly implicating the environment around F17 and/or F55) decreases significantly in this temperature range, while in the holoprotein (bound to oleic acid), this phenomenon is not observed. Concomitantly, an increase in the activity of binding to [^{14}C]oleic acid occurs. Nevertheless, other spectroscopic evidence indicates that the β-barrel structure, the major motif of this protein, is highly stable up to 70 °C. No changes associated with conformation were detected for both structures by fourth-derivative analysis of the UV absorption spectra, circular dichroism in the far-UV region, and intrinsic fluorescence measurements. Further structural information arises from experiments in which binding to the anionic fluorescent probes 1-anilinonaphthalene-8-sulfonic acid (ANS) and its dimer bisANS was examined. The fluorescence intensity of bound ANS diminishes monotonically, whereas that of bisANS increases slightly in the temperature range of 35−50 °C. Given the different size of these probes, model building suggests that ANS would be able to sense regions located deeply inside the cavity, while bisANS could also reach the vicinity of the small helical domain of this protein. In light of these results, we believe that this subtle conformational transition of IFABP, which positively influences the binding activity, would involve fluctuations at the peripheral "entry portal" region for the ligand. This interpretation is compatible with the discrete disorder observed in this place in apo-IFABP, as evidenced by NMR spectroscopy [Hodsdon, M. E., and Cistola, D. P. (1997) *Biochemistry 36*, 1450−1460].

Intracellular lipid binding proteins constitute a family of low-molecular mass proteins (12−15 kDa) with the putative general function of lipid trafficking (*1*). Members of this family include membrane fatty acid binding proteins (*2*, *3*), retinol binding proteins (*4*), retinoic acid binding proteins (*5*), sterol carrier proteins (*6*), and cytosolic fatty acid binding proteins (FABPs) (*7*). FABPs share a similar three-dimensional structure that resembles a clamshell and consists of 10 antiparallel β-strands arranged as two nearly orthogonal β-sheets with five strands each, enclosing a cavity which is the ligand binding site. The strands are mostly connected by tight turns except the first two, wherein β-strands are separated by a helix−turn−helix motif (*7*).

Escherichia coli-derived rat intestinal FABP (IFABP)[1] is one of the best studied members; this is a 131-amino acid residue protein suitable for bacterial expression and purification, since it contains neither proline nor cysteine residues, thus simplifying the folding mechanism, and therefore avoiding the formation of inclusion bodies (*8*). Its structure has been solved by X-ray crystallography and refined to 1.2 Å resolution in the apo form and to 1.75 Å with oleate bound (*9*, *10*). Recently, the NMR structure of these forms in solution has been elucidated (*11*−*13*). In holo-IFABP, the carboxylate of the bound fatty acid is buried deep inside IFABP where it interacts, through a hydrogen bond network, with two solvent molecules, the δ-guanidinium of R106 and the nitrogen of the indole group of W82. The structure of this protein differs from that of most known globular proteins, since its interior is occupied by a large solvent-filled cavity (~850 Å^3), displacing the hydrophobic core sideways.

In this work, we describe a reversible conformational change of IFABP triggered by temperature in the range of 30−50 °C, occurring well below the denaturation temperature of this protein (~75 °C). Aromatic residues as well as extrinsic fluorescent molecules were used as spectroscopic probes to monitor this transition. Differences were found between the apo and holo forms. We conclude that this

† This work was supported in part by grants from the National Research Council of Argentina (CONICET and SECYT), the University of Buenos Aires (UBACYT), Fundación Antorchas, and the European Union.

* To whom correspondence should be addressed.

[1] Abbreviations: ALBP, adipocyte lipid binding protein; ANS, 1-anilinonaphthalene-8-sulfonic acid; bisANS, 4,4′-dianilino-1,1′-binaphthyl-5,5′-disulfonic acid; CD, circular dichroism; DMSO, dimethyl sulfoxide; IFABP, intestinal fatty acid binding protein; IPTG, isopropyl β-D-thiogalactopyranoside; MD, molecular dynamics; NATA, *N*-acetyl-L-tryptophanamide; NMR, nuclear magnetic resonance; PDB, Brookhaven Protein Data Bank; rms, root-mean-square; SDS−PAGE, sodium dodecyl sulfate−polyacrylamide gel electrophoresis; Tris-HCl, tris(hydroxymethyl)aminomethane hydrochloride; $[\theta]_M$, molar ellipticity.

10.1021/bi981827x CCC: $15.00
Published on Web 11/05/1998

temperature-induced transition may reflect a subtle change in protein conformation, probably mapping to a peripheral region located near the helical hairpin motif, and positively influencing fatty acid binding activity.

MATERIALS AND METHODS

Materials. The pET11a expression vector was a gift from A. Kleinfeld (Medical Biology Institute, La Jolla, CA). This vector contains the ampicillin resistance gene and the rat IFABP cDNA under the control of phage T7 RNA polymerase. The BL21(DE3) *E. coli* strain was a gift from A. Kornblihtt (INGEBI, Buenos Aires, Argentina). This strain synthesizes T7 RNA polymerase when induced by IPTG. All chemicals for cell culture were purchased from Merck; buffers, NATA, ANS, and hydroxyalkoxypropyl dextran (Lipidex 1000) were purchased from Sigma, and [^{14}C]oleic acid was from Amersham Life Sciences. BisANS was kindly provided by A. A. Paladini (INGEBI).

Ligands. For binding assays, a fraction of a 50 μM freshly prepared solution of [^{14}C]oleic acid (50 μCi/μmol) in DMSO was diluted to the final concentration with 20 mM potassium phosphate buffer at pH 7.4 (buffer A) immediately before each experiment. The final DMSO concentration did not exceed 7% (v/v).

In experiments involving holo-IFABP, a solution of oleic acid in ethanol (4 mM) was used. IFABP and oleic acid at a 1:1 molar ratio were dissolved in buffer A. The final concentration of ethanol in the assay never exceeded 2%.

Solutions of bisANS or ANS were prepared in buffer A from 5 mM stock solutions in ethanol. The final concentration of each probe was calculated considering the following values for the extinction coefficients in water: 17 000 cm^{-1} M^{-1} (385 nm) for bisANS and 4950 cm^{-1} M^{-1} (350 nm) for ANS (*14*).

Purification of IFABP. Bacteria harboring the pET11a vector which carries the cDNA encoding IFABP were grown at 37 °C in Luria Broth medium (100 μg/mL ampicillin) until an A_{600nm} of 1.2 was achieved. IFABP was overexpressed by inducing phage T7 RNA polymerase in the host strain with IPTG (0.4 μM). After induction for 140 min at 37 °C, cells were harvested by centrifugation at 4000*g* over the course of 10 min at 4 °C and then kept at −20 °C for at least 24 h. Cells were lysed by a combined treatment with lysozyme and DNAse I following an established protocol (*15*).

Protein purification was achieved by the protocol described by Lowe et al. (*16*) with modifications. Basically, the procedure consists of (i) two consecutive ammonium sulfate precipitations at 30 and 70% saturation, after which the supernatant was saved; (ii) dialysis of the soluble material against 50 mM Tris-HCl buffer (pH 7.9); (iii) molecular filtration chromatography through a Sephadex G-100 column (93 cm × 2.7 cm) equilibrated in the same buffer; (iv) dialysis of the pooled fractions containing IFABP against 50 mM Tris-HCl (pH 9); and (v) anion exchange column chromatography (Whatman DE-52, 15.5 cm × 1.5 cm) in the same buffer. IFABP elutes in the middle of a 0 to 64 mM NaCl gradient. After dialysis against buffer A, the lipids were removed by passage through a Lipidex 1000 column (1 cm × 15 cm) warmed at 37 °C, according to Glatz and Veerkamp (*17*). The identity and the purity of the protein were assessed by (i) SDS−PAGE and staining with Coomassie Brillant Blue G, (ii) reversed phase HPLC in a C4 column, (iii) amino acid analysis after acidic hydrolysis, (iv) UV spectroscopy, and (v) far-UV CD. The concentration of IFABP in stock solutions was determined by its UV absorption measured in a JASCO 7850 spectrophotometer, considering a value for the extinction coefficients in water of 16 900 cm^{-1} M^{-1} (280 nm) (*18*).

Ligand Binding Activity. For experiments intended to assay the ligand binding activity of IFABP as a function of temperature, the protocol described by Glatz and Veerkamp (*17*) was followed. Results were expressed as the ratio of radioactivity bound to the total radioactivity added to the sample (*B*/*T*). The bound radioactivity (in counts per minute) represents the amount of [^{14}C]oleic acid found in the supernatant after incubation of IFABP with this ligand over the course of 10 min at each temperature assayed, followed by the addition of Lipidex 1000 and subsequent centrifugation of the suspension at 0 °C. Control samples did not contain protein. On the other hand, radioactivity of a 2 μM [^{14}C]oleic acid solution was also measured as a function of temperature to estimate eventual losses due to differential adsorption of the fatty acid to the glass walls. This value did not vary by more than 10% in the range of 20−70 °C.

Circular Dichroism Spectra. Spectra were recorded on a JASCO J-20 spectropolarimeter employing thermostated cuvettes connected to a circulating water bath (Haake). The temperature of the sample was measured directly in the cuvette with the aid of an electronic thermocouple. Spectra in the near-UV region (between 245 and 310 nm) or in the far-UV region (between 200 and 250 nm) were collected using a cuvette with a 100 or 1 mm path length, respectively, closed with Teflon caps. The scanning speed was 5 nm/min, and the time constant was 4 s. Four consecutive scans were taken for each sample, and the data were averaged to reduce noise. Delipidated IFABP (apo-IFABP) or holo-IFABP (20−40 μM) dissolved in buffer A was used. Data were converted to molar ellipticity $[\theta]_M$ (in units of deg cm^2 dmol^{-1}) using a mean residue weight value of 110.68 g/mol.

Fourth-Derivative UV Spectra. Spectral data were collected on a JASCO 7850 spectrophotometer, using a 1 cm path length thermostated cuvette connected to a circulating water bath (Haake). The temperature of the sample was measured directly in the cuvette with the aid of an electronic thermocouple. The cuvette was sealed with a Teflon cap to avoid evaporation. The scanning parameters were a spectral bandwidth of 1 nm and a scan speed of 40 nm/min. Spectra were recorded in the range between 250 and 320 nm. Fourth-derivative spectra were numerically calculated with the built-in program provided with the spectrophotometer, considering a data interval of 10 nm. The protein concentration of the sample varied between 20 and 50 μM. To minimize light scattering, samples were filtered through a 0.22 μm Millipore Millex-GV membrane immediately before measurements.

Fluorescence Measurements. Fluorescence emission spectra were recorded on a SLM AMINCO 4800 spectrofluorometer equipped with a thermostated holder connected to a circulating water bath. A 1 cm path length cuvette sealed with a Teflon cap was used. The temperature was measured directly with an electronic thermocouple immersed in the sample. For measurements of intrinsic fluorescence spectra

of tryptophan, the following parameters were set: excitation and emission slits of 4 nm, an excitation wavelength of 295 nm, and an emission range of 320−450 nm. The protein concentration was 7 μM. For fluorescent probes bisANS or ANS, excitation wavelengths were 400 and 380 nm, respectively, and emission was collected in the range of 420−600 nm. IFABP (10 μM) dissolved in buffer A was incubated with each of these extrinsic probes at the temperatures indicated in each case. Data were corrected by the fluorescence intensity of rhodamine to account for possible changes in the intensity of the lamp during the assay and by inner filter effects according to Lakowicz (*19*). To minimize light scattering, samples were filtered through a 0.22 μm Millipore Millex-GV membrane before each experiment. For each spectrum, the center of mass $\langle \nu_p \rangle$ (in cm^{-1}) was calculated according to Weber (*20*):

$$\langle \nu_p \rangle = \sum \nu_i F_i / \sum F_i$$

where F represents the relative fluorescence intensity and ν is the wavenumber ($\nu = 1/\lambda$) at wavelength i. The wavelength of the center of mass (in nm) is then calculated ($\lambda_p = 10^7/\langle \nu_p \rangle$).

Molecular Modeling. Modeling of ANS or bisANS within the binding cavity of IFABP, including the calculation of torsion angles, volumes, distances, and solvent accessible surface areas, was carried out with MacroModel 5.5 and BatchMin 5.5 (*21*) installed on a Silicon Graphics O2 computer (R10000, 320 MB RAM, 4 GB hard disk) under the Irix 6.3 operating system. We used the MM2* force field (the version of Allinger's MM2 force field as implemented in MacroModel). By default, atomic partial charges were calculated from data in the molecular mechanics force field chosen. MM2* force field uses distance-dependent dielectric electrostatics, instead of the standard dipole−dipole electrostatics. The conformational search of ANS and bisANS was carried out following an optimized Monte Carlo method (*22*). For technical reasons, the calculation was carried out neglecting the ionization of the functional groups. The electrostatic interaction cutoff was set to 50 Å. For energy minimization, we used a conjugate gradient method, with a final gradient of 0.05 kJ $Å^{-1}$ mol^{-1} (0.01 kcal $Å^{-1}$ mol^{-1}) as the criterion for convergence. After the Monte Carlo steps, initial conformers were partially minimized (250 iterations), and the subsets of resulting structures were further minimized until convergence. In this process, duplicate and high-energy structures were discarded. In the end, all nonenantiomeric conformers, within a 25 kJ/mol (6 kcal/mol) window above the global minimum, were tabulated.

Data for Ramachandran-like plots were obtained by driving dihedral angle rotation around $\Phi_1 - \Phi_2$ in ANS and $\Phi_1 - \Phi_5$ in bisANS (see Figure 7) using the MacroModel DRIV command implemented in a BatchMin routine. Initially, structures corresponding to the global minima of ANS and bisANS were located within the cavity of IFABP by performing a rigid-body superimposition of these ligands with atomic coordinates of bound palmitic acid taken from the PDB file of holo-IFABP (PDB code 2ifb; *9*). In the end, energy minimization (using MM2*) of the bound conformers was achieved considering the binding pocket of IFABP as a rigid substructure including all atoms within 6 Å of the ligand.

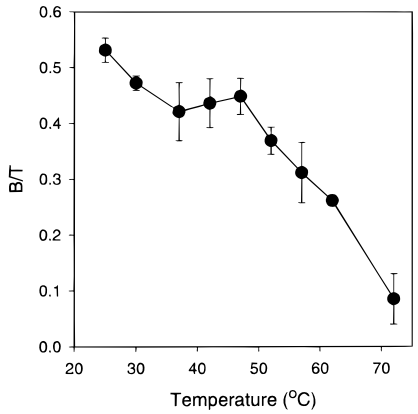

FIGURE 1: Binding activity of IFABP to oleic acid as a function of temperature. Oleic acid (2 μM) was incubated with IFABP (2 μM) as described in Materials and Methods. *B*/*T* represents the ratio between bound and total oleic acid in the sample. Each point represents the average of three independent experiments, each of which was performed in triplicate. The standard error of each experimental point is represented by vertical bars.

To study the stability of the complexes calculated after energy minimization, MD simulations were run at 300 K in vacuo. The cutoff distance for electrostatic interactions was also set to 50 Å. In all cases, the simulation was run 200 ps after an initial equilibration time of 50 ps. A time step of 1.5 fs was used. Like the case for the procedure for the energy minimization of the ligand within the cavity described above, only the ligand was allowed to move. A hydrogen bond NH···O═S is considered to be formed whenever (i) the distance between the acceptor and donor is smaller than 2.5 Å, (ii) the angle N−H···O(═S) is greater than 120°, and (iii) the angle (N)H···O═S is greater than 90°.

RESULTS

Activity of Binding of IFABP to [^{14}C]Oleic Acid. Binding of oleic acid to IFABP at each temperature was assayed by the Lipidex method, as described in Materials and Methods. This activity was found to diminish as temperature rises (Figure 1), consistent with an exothermic reaction, as was observed before employing a fluorescent assay based on an acrylodan-modified form of IFABP (*23*, *24*). However, we noticed a deviation from this general behavior starting at ∼35 °C where the extent of binding increases significantly. This effect is most noticeable between 35 and 50 °C, and persists beyond this range up to 60−70 °C.

To gain structural information on the origin of this enhanced activity, we carried out spectroscopic analyses of IFABP in the presence or in the absence of the natural ligand oleic acid as a function of temperature.

Circular Dichroism. Near-UV CD spectra (245−310 nm) of IFABP were collected in the temperature range of 20−60 °C. Perturbations in the chiral environment around aromatic residues can be detected by studying changes in this region. The spectrum at 22 °C (Figure 2A) shows signals located in three main regions, namely, 245−265 and 290−305 nm, where positive bands appear, and 265−290 nm, where negative bands are observed. Three major positive bands (with maxima at 248, 254, and 260 nm), of which the second one is the strongest, were resolved in the first region. In apo-IFABP, a generalized flattening of the

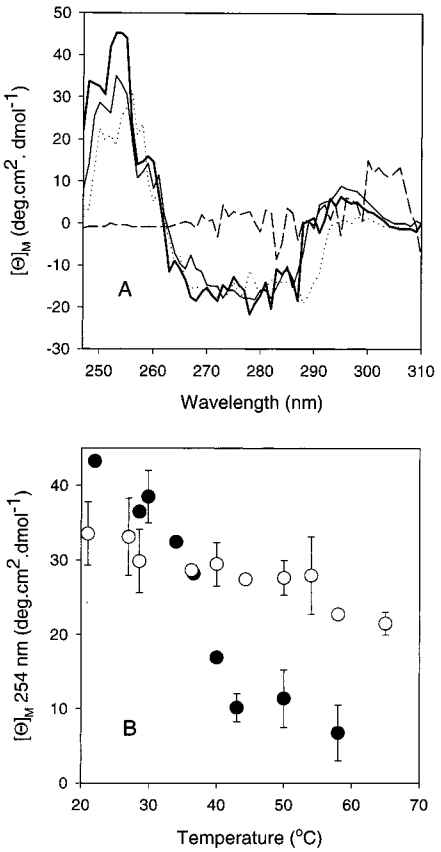

FIGURE 2: (A) Circular dichroism spectra in the near-UV region of apo- and holo-IFABP. IFABP (20−40 μM) was dissolved in 20 mM potassium phosphate buffer (pH 7.4), and the spectra recorded at 22 °C (bold line, apo; light line, holo) and 50 °C (dashed line, apo; dotted line, holo) are shown. (B) Molar ellipticity at 254 nm of apo (●)- and holo-IFABP (○) as a function of temperature. Each point represents the average of two independent experiments, each of which was in turn the average of at least four scans.

spectrum occurs with increasing temperatures (Figure 2A). Most remarkably, a significant decrease in molar ellipticity at 254 nm ($[\theta]_{M_{254nm}}$) is observed, a band tentatively assigned to the environment of phenylalanine residues (*25*). Although histidine residues could in principle also contribute to this spectral region (*26*), here the chance is minimal given the fact that the molar ratio of H:F is 1:8. The transition occurring between 30 and 45 °C (Figure 2B) was found to be reversible (no hysteresis was observed, data not shown). A sample heated to 45 °C and then gradually cooled to 22 °C showed a spectrum indistinguishable from the original one. In particular, the temperature-dependent obliteration of the negative bands in the range of 265−290 nm reflects the possibility that changes in the environment of other aromatic residues (tyrosine and/or tryptophan) might also be taking place.

In the presence of oleic acid, a natural ligand of IFABP, the near-UV CD spectrum at 22 °C does not differ significantly from that of apo-IFABP (Figure 2A). However, when assayed as a function of temperature, the CD spectrum of holo-IFABP remains almost unchanged until 65 °C (Figure 2A). Correspondingly, no transition was observed by following the ellipticity at 254 nm (Figure 2B).

On the other hand, the far-UV CD spectrum (200−245 nm) was also examined in the same temperature range. Unlike the behavior described above, here no variation was found up to 75 °C (data not shown), as judged by the ellipticity at 216 nm, a wavelength indicative of the predominant content of β-sheet structure which characterizes this protein.

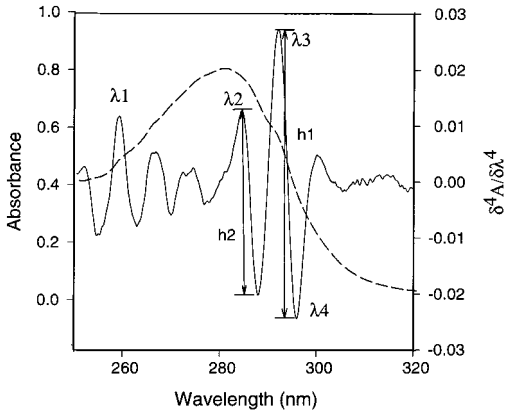

FIGURE 3: Zero-order (- - -) and fourth-derivative absorption spectra (—) of apo-IFABP. IFABP (20−50 μM) was dissolved in 20 mM potassium phosphate buffer (pH 7.4), and the spectrum was recorded at 22 °C. Characteristic wavelengths λ_1−λ_4 and valley-to-peak distances h_1 and h_2 are shown.

Fourth-Derivative UV Spectra. Figure 3 shows both zero- and fourth-order UV absorption spectra of apo-IFABP at 22 °C. This analysis enhances features present in the original absorption spectrum and allows us to distinguish peaks and shoulders more clearly. Maxima in the fourth-derivative spectrum correspond to maxima in the zero-order absorption spectrum. Two main regions of interest were analyzed: the 255−265 nm interval, where signals of phenylalanine appear (centered around λ_1), and the 280−300 nm interval, where bands arising from electronic transitions of tyrosine and tryptophan occur (with characteristic wavelengths λ_2−λ_4). λ_4 is mostly influenced by the environment of tryptophan, since the contribution of tyrosine becomes negligible, as long as the molar ratio of W:Y is 1:4 or greater (this ratio is 2:5 for IFABP). Values of λ_4 greater than 293 nm are indicative of the exposure of W residues to a nonaqueous environment (*27*). For IFABP, λ_4 is ∼295.0 nm at 20 °C, suggesting hydrophobic surroundings for W residues. On the basis of the crystallographic structure of IFABP (*9*), the calculation of the solvent accessible surface area of W6 and W82 agrees with this observation; the values obtained were 0 and 0.7 Å^2, respectively, assuming a radius of 1.4 Å for the water molecule probe. As the temperature rises from 30 to 50 °C, a reversible overall red shift (implying a more hydrophobic milieu), albeit of a small magnitude (∼0.2−0.3 nm), was observed at all characteristic wavelengths measured (Figure 4A−C). All curves plateau above 50 °C and up to 70 °C. Most remarkably, no blue shift is observed in the temperature range studied, a phenomenon generally associated with an increased exposure of aromatic residues to an aqueous environment occurring upon protein denaturation. Besides, no significant increase in the extent of light scattering occurs, as monitored by measurements of turbidity (UV absorption at 320 nm), thus ruling out any effect due to protein aggregation (data not shown). Unlike the situation described so far, at temperatures >70 °C the extent of light scattering increases dramatically and is indeed accompanied by the characteristic blue shift associated with protein unfolding. No significant difference between apo- and holo-IFABP was

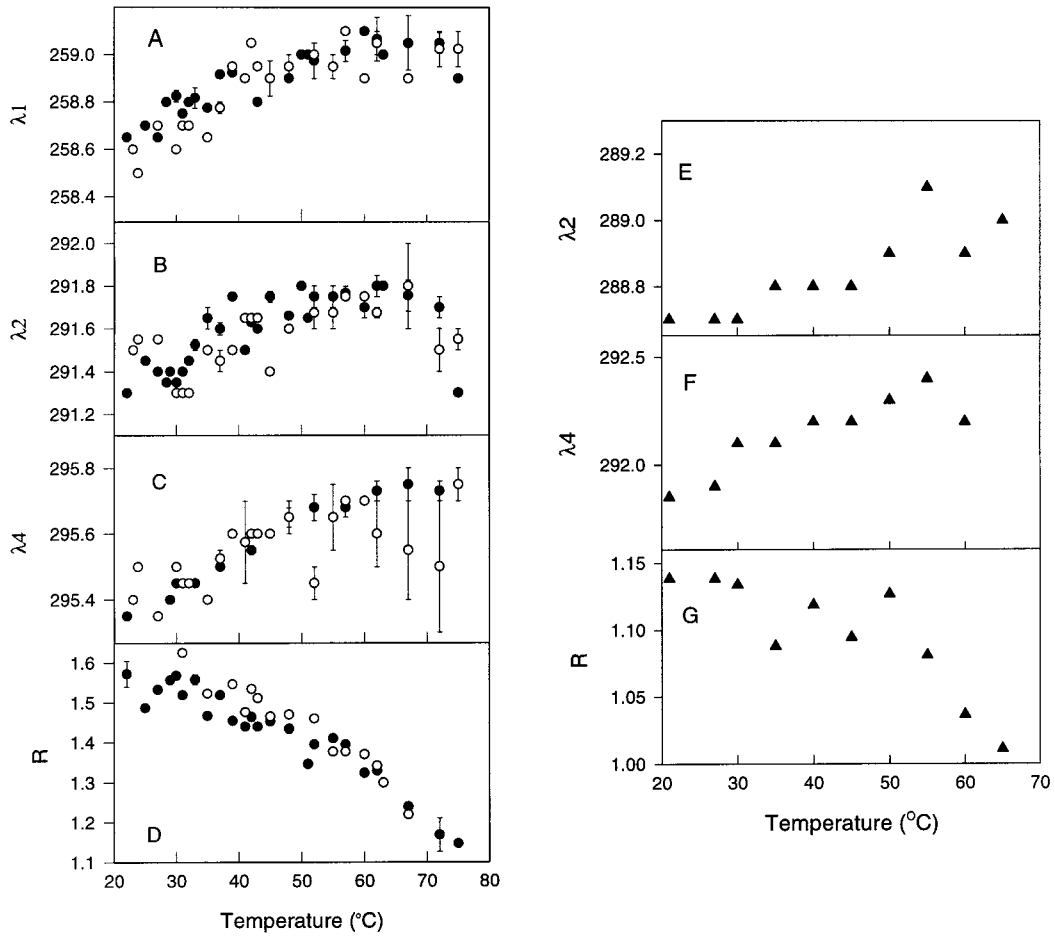

FIGURE 4: Characteristic wavelengths derived from the fourth-derivative analysis of the absorption spectra of apo (●)- and holo-IFABP (○) as a function of temperature (A−D). The following parameters are plotted: λ_1, λ_2, λ_4, and the parameter R, calculated as the ratio between amplitudes h_1 and h_2 (see Figure 3). The average (±standard deviation) of three to five independent experiments is shown. Panels E−G represent the results from a parallel experiment with NATA (100 μM) run under the same experimental conditions.

observed when λ_1, λ_2, and λ_4 were studied as a function of temperature (Figure 4A−C).

On the other hand, the parameter R, the ratio between peak to valley distances h_1 and h_2 of signals in the range of 280−295 nm (Figure 3), was calculated at each temperature assayed. The absolute value of R varies between 1.4 and 1.6 in the temperature range where the transition takes place (Figure 4D); these values are comparable with those found for other proteins (*27*). Apo- and holo-IFABP show almost superimposable curves, showing a steady tendency toward lower values as the temperature increases. Significantly, no maximum was observed at the midpoint of the transition (∼40 °C), a feature generally apparent in denaturation equilibria (*27*, *28*). By contrast, at higher temperatures R indeed varies abruptly as temperature approaches T_m (74 °C) (data not shown).

To evaluate the significance of the change observed with regard to the protein conformation, we analyzed the spectrum of NATA in the same temperature range. A red shift of a similar magnitude was observed for this model compound (Figure 4E−G), thus indicating that this drift arises mainly as a consequence of the thermally induced decrease in the polarity of the solvent due to higher disorder of the water cage around the indole ring.

Fluorescence Measurements. When IFABP is excited at 295 nm, the maximum of fluorescence emission occurs at 330 (apo form) or 328 nm (holo form), suggesting that at least one tryptophan residue resides in a nonpolar environment. This notion agrees well with conclusions drawn from fourth-derivative analysis of the UV absorption spectrum (λ_4 value) and is consistent with the hydrophobic environment observed for these residues. The fluorescence emission spectra of tryptophan residues (300 and 450 nm) were collected in the temperature range of 22−75 °C. The following parameters were analyzed: (i) the wavelength of the center of mass of the fluorescence spectrum and (ii) the fluorescence intensity at 330 nm as a function of temperature (panels A and B of Figure 5, respectively).

In apo-IFABP, the wavelength of the center of mass (or the wavelength of the fluorescence emission maximum, result not shown) remained constant as a function of temperature up to 70 °C. Beyond this temperature, an abrupt red shift occurred as a consequence of the exposure of tryptophan residues to the aqueous phase upon protein unfolding. The fluorescence emission maximum of holo-IFABP is blue shifted compared to that of the apo structure. Probably, the presence of oleic acid in the cavity is responsible for this effect, since W82 is known to interact with the carbon backbone of the fatty acid and the indole NH is hydrogen bonded to an oxygen atom of the fatty acid carboxylate group (*29*). The behavior of the wavelength of maximum emission as a function of temperature is similar to that of the apo structure, except at high temperatures where the red shift occurs (above 75 °C, Figure 5A). This suggests an increase

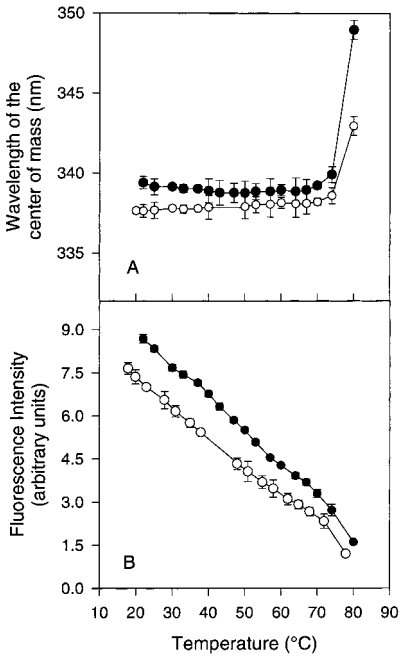

FIGURE 5: (A) Wavelength of the center of mass of the fluorescence spectrum of apo (●)- and holo-IFABP (○) as a function of temperature. This parameter was calculated as described in Materials and Methods. Apo- or holo-IFABP (7 μM) dissolved in 20 mM potassium phosphate buffer (pH 7.4) was excited at 295 nm, and the emission intensity was collected in the range of 320−450 nm. (B) Fluorescence intensity at 330 nm of apo (●)- and holo-IFABP (○) as a function of temperature.

in the stability of the protein determined by the presence of the ligand within the binding cavity. On the other hand, fluorescence intensity monotonically diminishes along this temperature range (Figure 5B), reflecting the characteristic dependence of tryptophan fluorescence upon temperature increase (*30*).

In the absence of any difference in the intrinsic fluorescence of IFABP at temperatures below 70 °C, measurements in the presence of the extrinsic fluorescent probes ANS or its dimer bisANS were also carried out to obtain additional information on a putative conformational change. Both molecules are very sensitive to a variation in the polarity of the environment; namely, their fluorescence is highly enhanced as the polarity of the solvent decreases (*31*). We found that IFABP binds both ANS and bisANS. In addition, we showed that oleic acid was indeed able to displace ANS or bisANS from its binding site in IFABP. The estimated dissociation constants for these fluorescent ligands at 37 °C were 16.0 ± 1.7 and 8.6 ± 2.9 μM, respectively (data not shown). The fluorescence of each of these probes bound to IFABP was measured as a function of temperature (Figure 6). While the fluorescence intensity of bound ANS decreased monotonically upon increasing the temperature, the behavior of bound bisANS showed a departure from linearity between 35 and ∼55 °C; i.e., the fluorescence intensity remained almost constant in this range, while the expected decrease occurs at lower and higher temperatures. Remarkably, this temperature range overlaps with that where the transition was observed by CD (Figure 2B) and with the region where enhanced binding of oleic acid occurs (Figure 1). Each probe dissolved in 1-butanol showed a monotonic decay of fluorescence emission as temperature rises (Figure 6, inset), suggesting that bisANS per se is not responsible

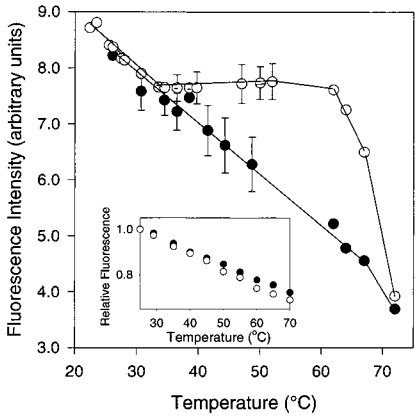

FIGURE 6: Fluorescence intensity of ANS (●) and bisANS (○) bound to IFABP as a function of temperature. ANS or bisANS (10 μM) incubated with apo-IFABP (10 μM) dissolved in 20 mM potassium phosphate buffer (pH 7.4) was excited at 380 or 400 nm, respectively. The emission intensity was monitored at 490 nm. The inset shows the relative fluorescence intensity of ANS (●) or bisANS (○) (10 μM) dissolved in 1-butanol measured under the same conditions.

for the anomaly found when bound to IFABP; rather, this probe could be revealing a temperature-induced conformational change of this protein. The overall behavior could be interpreted as an enhancement of fluorescence superimposed over the expected thermal quenching process.

Molecular Modeling. To evaluate the feasibility of formation of complexes between ANS or bisANS and IFABP, we built molecular models employing MacroModel 5.5 (*21*). We proceeded as follows. (i) A conformational search in vacuo of both ligands in their free forms was carried out with an optimized Monte Carlo procedure (*22*). (ii) Fitting of the minimum energy conformers into the binding pocket of IFABP was achieved by manual docking. (iii) Finally, these complexes were refined by constrained energy minimization, and the stability of the final models was evaluated by MD simulations.

Molecular models of ANS and bisANS were initially constructed using the model-building facility implemented in MacroModel. Coordinates of these structures were later used as input for BatchMin, the calculation module of this program. To search the conformational space available to these compounds, we ran an optimized Monte Carlo procedure which allows free rotation around dihedral angles that constitute the major determinants of the structure, i.e., $\Phi_1 - \Phi_2$ and $\Phi_1 - \Phi_5$ for ANS and bisANS, respectively (see Figure 7A). Planar structures were used as starting geometries. Conformers corresponding to the energy minima (as calculated with the force field MM2*) within a 25 kJ/mol (6 kcal/mol) window above the global minimum are listed in Table 1.

For ANS, a single nonenantiomeric conformer was obtained. An intramolecular NH···OS hydrogen bond is predicted, although, due to steric hindrance between substituents in the naphthalene ring, the geometry is far from ideal; e.g., the bond angle N−H···O is 118°. Structural data for ANS show wide variability of Φ_1/Φ_2 depending on the crystallographic and chemical form (acid or salt) of the compound (*32*−*34*). This behavior is consistent with the extended width of the energy wells, as revealed by Ramachandran-like plots (results not shown). In this regard, the

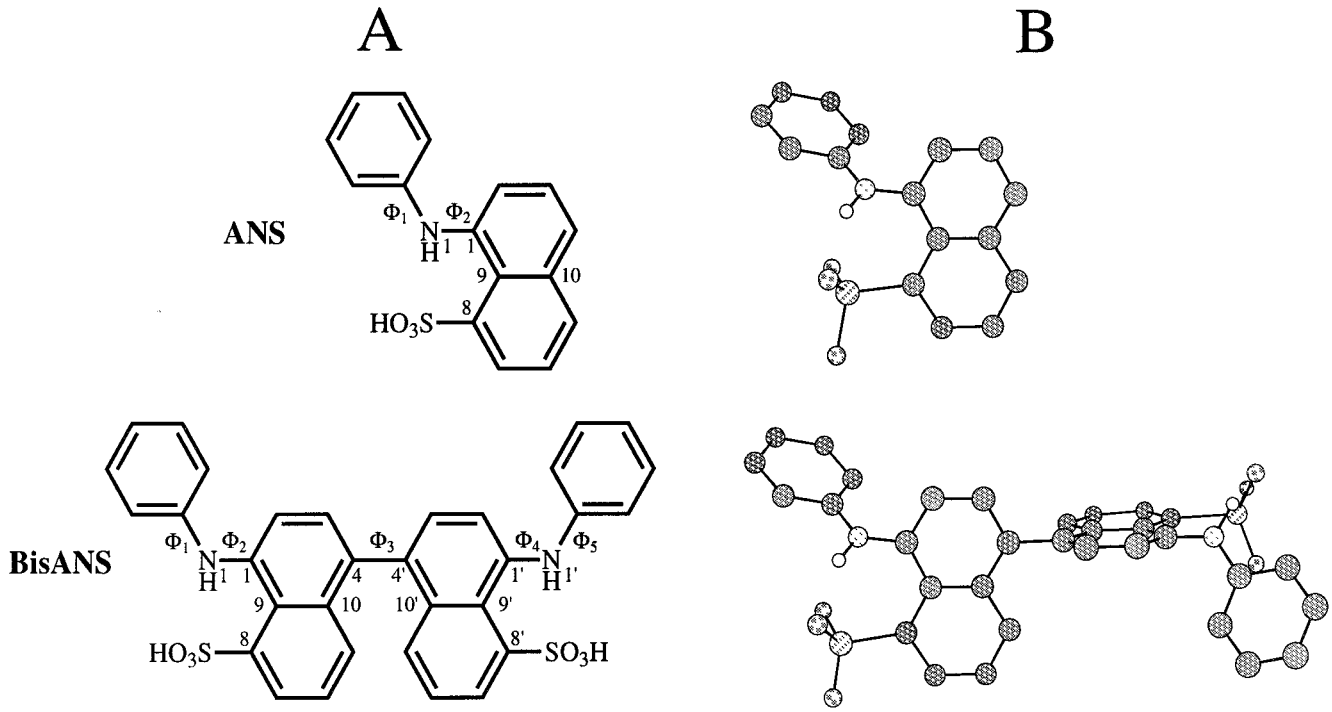

FIGURE 7: (A) Structures of ANS and bisANS showing the torsion angles determining the conformation. The definition of dihedral angles follows the convention: Φ_1, C−C−N_1−C_1; Φ_2, C−N_1−C_1−C_9; Φ_3, C_{10}−C_4−$C_{4'}$−$C_{10'}$; Φ_4, C−$N_{1'}$−$C_{1'}$−$C_{9'}$; and Φ_5, C−C−$N_{1'}$−$C_{1'}$. (B) Ball-and-stick conformational representation of the global minimum energy conformers of each of these compounds found after the optimized Monte Carlo search.

Table 1: Dihedral Angles and Energy Differences between Conformers Corresponding to Energy Minima of ANS and BisANS after a Monte Carlo Simulation

	ANS		
		conformer **1**	
dihedral angle (deg)[a]			
Φ_1		14.6	
Φ_2		−118.1	
	BisANS		
	conformer **1**	conformer **2**	conformer **3**
dihedral angle (deg)[a]			
Φ_1	13.5	13.6	13.8
Φ_2	−119.8	−120.1	−120.3
Φ_3	83.7	−81.3	−82.1
Φ_4	−119.9	−120.1	116.6
Φ_5	12.2	12.2	−10.7
Δenergy[b] (kJ/mol)	0	0.63	4.97

[a] The definition of dihedral angles follows the convention described in the legend of Figure 7A. [b] The difference in energy relative to the global minimum is shown.

Φ_1/Φ_2 pair found for a crystal structure of ammonium ANS hemihydrate (−9°/134° for crystal structure **2**; *33*) agrees well with that found for the enantiomer of the minimum energy conformer (−15°/118°, Table 1). In addition, the range of dihedral angles between the phenyl and naphthalene rings observed among different crystal forms (53−63°; *32*) falls close to the value found for conformer **1** (67°).

On the other hand, not unexpectedly, the dihedral angles determining the conformation of each half of bisANS coincide with those found for the global minimum of ANS (Table 1). Only two values are allowed for the central torsion angle (Φ_3), which place the plane of naphthalene rings almost normal to each other. Consequently, three energy-minimized conformers were found for bisANS. As for the calculated ANS structure, in all cases, intramolecular NH···OS hydrogen bonds are predicted. Models of the conformers corresponding to the global minimum of each compound are shown in Figure 7B.

Next, we undertook the task of modeling the conformers of each fluorophore within the binding cavity of IFABP. A framework including the amino acid residues comprising the walls of the binding cavity in IFABP was considered for fitting the fluorescent ligands ANS or bisANS. As a first approximation, each minimum energy conformer was superimposed as a rigid body on the carbon skeleton of palmitate bound to IFABP, based on the known structure of this complex (*9*). For this task, high priority was given to the spatial coincidence of the sulfonate group of the ligands with the carboxylate group of palmitate (the distance between the carboxylate oxygen and a guanido hydrogen of R106 is 1.65 Å). In the crystal structure of holo-IFABP, palmitate kinks at C_4−C_7. After visual inspection, the plane defined by this bend appeared to be an appropriate target for fitting the naphthalene ring. If necessary, the ligand was translated as a rigid body to prevent obvious atomic clashes with residues lining the binding cavity. After these procedures, all models complied with the requirement that the sulfonate group lie at hydrogen bonding distance from the guanido group of R106. When it is considered that the cavity is asymmetric and disk-shaped, ligands exhibiting two distinct faces can be accommodated in two different positions. For ANS, the added restriction imposed by the hydrogen bond allows only two possible binding modes for each enantiomer of each conformer, resulting in four tentative models. On the other hand, for bisANS, one should also consider that one or the other sulfonate group could be anchored to R106. However, given the internal symmetry of this molecule, the set of possible binding modes is reduced to 10.

The invariance in the orientation of side chains of inner residues in the β-barrel structure by comparison of apo and holo forms of IFABP, as revealed by X-ray crystallographic and NMR studies (*9*−*13*), allowed us to model the binding interaction maintaining fixed the protein framework and moving only the ligand within the cavity.

The following criteria were adopted for the acceptance of the most likely models of bound ANS or bisANS to IFABP: complexes for which (i) the energy is within a 100 kJ/mol window above the global minimum and (ii) the energy is lower than that calculated after translation of the ligand out of the cavity (protein and ligand separated by ∼100 Å).

When bound, each conformer of ANS yielded structures **1b** and **1′b** which exhibited dihedral angles within the same energetic well in a Φ_1/Φ_2 Ramachandran-like plot as the corresponding free form **1** (data not shown). This fact is reflected in the small rms difference between bound and free forms of the ligand (0.44−0.62 Å, Table 2). Both conformers met the criteria stated above, conformer **1′b** exhibiting the lowest energy, mainly due to better van der Waals interactions. Intramolecular hydrogen bonds persist in bound conformers of ANS.

On the other hand, there is a wider energy difference for bound bisANS forms. Among these models, only models **1b**, **2b**, and **3′b**↑ met the selection criteria (Table 2). As for ANS models, rms differences between bound and free forms are not high (<1.5 Å). The angular deviations between torsion angles calculated for bound and free forms of bisANS are larger than those measured for ANS, implying that a tighter constraint imposed by the size and shape of the cavity exists for the former. In any case, all torsion angles Φ_i map in the same low-energy regions in Ramachandran-like plots. Here, the extent of hydrogen bonding differs among conformers. For example, **1b** forms both hydrogen bonds, only the distal NH···OS bond is shown in **2b**, and no bond was predicted for **3′b**↑. However, due to the existence of water molecules within the binding cavity (*9*, *10*), intermolecular water hydrogen bonds bridging the ligand with residues lining the walls could well compensate for the loss of intramolecular hydrogen bonding.

The best models for ANS (**1′b**) or bisANS (**2b**) bound to the cavity of IFABP are represented in Figure 8. To test the snug fit of each conformer within the binding cavity, a manual translation (±1 Å) of the ligand along all three coordinate axes followed by energy calculation was performed. In all cases, the energy increased dramatically (by at least 200 kJ/mol) due to steric clashes. Results from this test agree well with those derived from the calculation of the volume common to both the ligands and the cavity. There is no significant overlap between ANS or bisANS and amino acid side chains lining the walls of the cavity (<5%). In any case, we anticipate that the extent of overlap could well be eliminated by minimal local motions of these side chains. On the other hand, superimposition between bound conformers of ANS or bisANS is significant, 63 and 55−58%, respectively, implying a general common environment for these molecules within the binding cavity.

Finally, MD simulations of the chosen models (a 200 ps run where only the ligand was allowed to move) were carried out to evaluate the stability of the complexes. The most frequent values of dihedral angles (Φ_i) and interatomic distances (between the ligand and residues of the protein) found along the MD run are reported in Table 3. For comparison, deviations of angles from average values were also calculated for palmitic acid in its free and bound forms.

Table 2: Conformations Corresponding to Energy Minima of ANS and BisANS after Minimization within the Binding Cavity of IFABP[a]

	ANS	
	conformer **1b**	conformer **1′b**
dihedral angle (deg)		
Φ_1	4.6	−4.7
Φ_2	−107.2	105.2
Δenergy$_{conf}$ (kJ/mol)[b]	73.8	0
Δenergy$_{free-bound}$ (kJ/mol)[c]	98.6	29.9
distance (Å)		
NH_{R106}···OS_8 hydrogen bond	2.03	3.00
phenyl$_{F55}$−phenyl[d]	13.10	13.60
$Cz_{F55}-C_{10}$	8.58	7.90
$Cz_{F55}-N_1$	11.14	11.57
$C\gamma_{D34}$−phenyl[d]	12.18	12.25
$C\gamma_{D34}-C_{10}$	6.49	6.70
$C\gamma_{D34}-N_1$	9.83	9.70
$C\alpha_{K27}$−phenyl[d]	15.81	16.47
$C\alpha_{K27}-C_{10}$	11.88	11.11
$C\alpha_{K27}-N_1$	14.32	14.56
rms (Å)[e]	0.624	0.438
volume (Å^3)[f]	249	248
overlapping volume (%)[f]	4.0	1.2

	BisANS		
	conformer **1b**	conformer **2b**	conformer **3′b**↑
dihedral angle (deg)			
Φ_1	65.8	57.8	14.2
Φ_2	−143.4	−124.0	65.9
Φ_3	110.4	−42.6	43.6
Φ_4	−131.9	−99.9	−75.0
Φ_5	35.7	−13.0	−34.4
Δenergy$_{conf}$ (kJ/mol)[b]	100.0	0	79.8
Δenergy$_{free-bound}$ (kJ/mol)[c]	33.9	149.0	84.4
distance (Å)			
NH_{R106}···OS_8 hydrogen bond	1.72	1.94	2.13
phenyl$_{F55}$−phenyl[g]	4.87	5.62	4.52
$Cz_{F55}-C_{9'}$	9.17	6.68	6.67
$Cz_{F55}-N_{1'}$	6.73	5.91	5.84
$C\gamma_{D34}$−phenyl[g]	7.35	7.67	7.79
$C\gamma_{D34}-C_{9'}$	8.18	5.68	6.44
$C\gamma_{D34}-N_{1'}$	8.25	6.03	7.52
$C\alpha_{K27}$−phenyl[g]	5.67	6.15	5.06
$C\alpha_{K27}-C_{9'}$	10.91	10.11	9.09
$C\alpha_{K27}-N_{1'}$	8.08	8.25	6.97
rms (Å)[e]	1.06	1.35	1.56
volume (Å^3)[f]	476	472	475
overlapping volume (%)[f]	5.0	4.0	4.8

[a] The nomenclature of conformers is as follows. The number refers to the original conformer (Table 1) which was fitted into the cavity; the prime (′) indicates the enantiomer of the corresponding conformer, and b is for bound. The up arrow indicates the orientation of each sulfonate group in bisANS relative to R106. In all cases, the dihedral angles Φ_1 and Φ_2 belong to the hemimolecule that is closer to R106. [b] The difference in energy relative to the structure with the lowest energy is shown. [c] The difference in energy between the ligand separated 100 Å from the protein relative to that of the bound form. [d] Distances between the centers of mass of such rings. [e] Rms deviation (in angstroms) calculated after a rigid-body superimposition between the starting and final conformer structure. The planarity of the aromatic rings was maintained by restraining torsions around these cycles to the values of the minimized conformers in vacuo within a ±2.5° range. [f] Total van der Waals volume of the ligand. The overlapping volume between the ligands and residues belonging to the binding cavity is indicated relative to the total volume of the ligand (%). [g] Distance measured from the center of mass of the phenyl ring belonging to the hemimolecule of bisANS that is closer to the indicated residue atom.

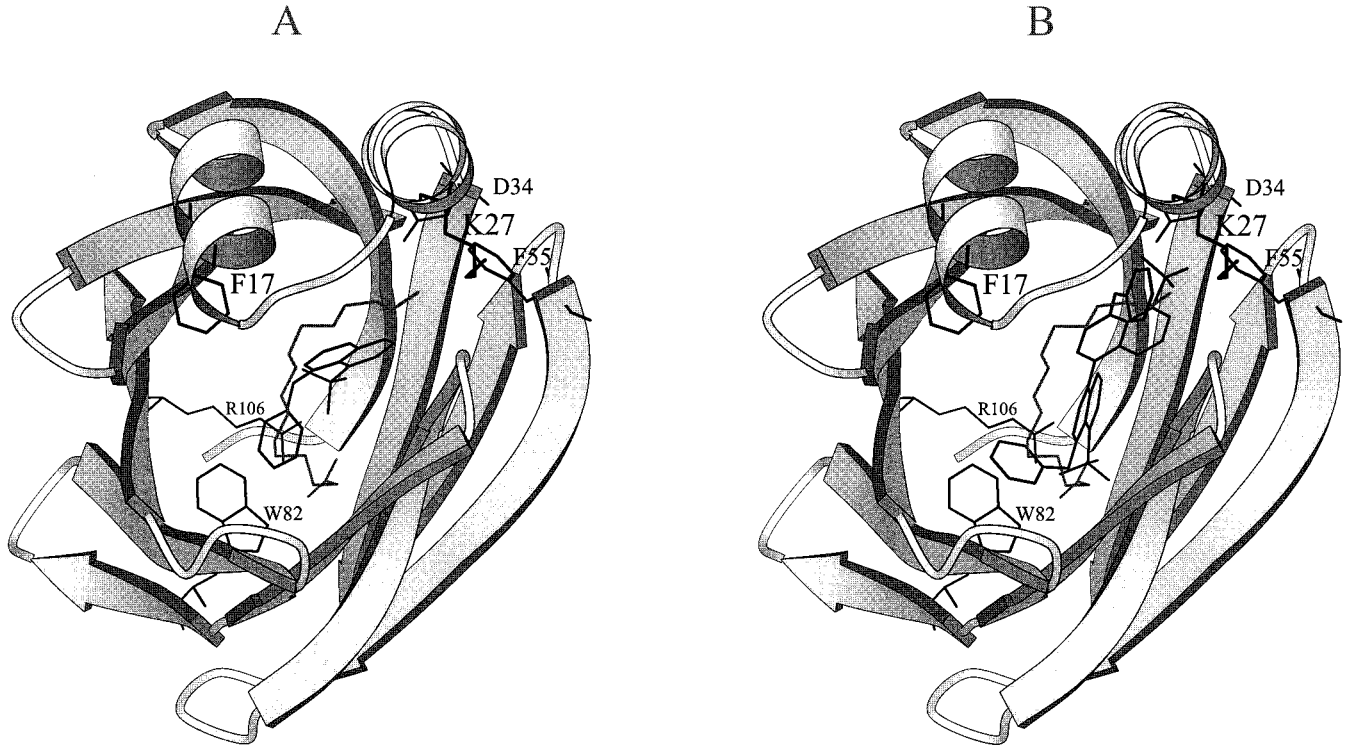

FIGURE 8: Schematic view of ANS (A) and bisANS (B) bound to IFABP. Coordinates of models **1′b** and **2b** (Table 2), respectively, superimposed with the experimentally determined structure of palmitic acid (in gray) bound to the protein (2ifb; *9*) were used as input to generate this figure with the program MOLSCRIPT (version 1.4; *44*). Relevant amino acid side chains mentioned in the text are also represented.

Not unexpectedly, several dihedral angles along the aliphatic chain in the free form of palmitic acid undergo abrupt transitions between trans (180 ± 25°) and gauche (−55 ± 15° and 70 ± 20°) conformations, e.g., the C_3-C_4 and $C_{13}-C_{14}$ torsions. By contrast, the constraint imposed by the binding cavity precludes the bound form from experiencing this transition; i.e., a monomodal and sharper distribution of these torsions was found (C_3-C_4 torsion = 167.9 ± 4.5° and $C_{13}-C_{14}$ torsion = −78.7 ± 5.6°). Similarly, both ANS and bisANS exhibited a narrower distribution of torsion angles in their bound forms as compared to their free forms (Table 3). In addition, the average values for these angles and interatomic distances between the ligands and characteristic amino acid residues lining the cavity do not differ significantly from those calculated in the energy-minimized complexes (compare values in Tables 2 and 3).

DISCUSSION

An Enhancement of the Binding Activity of IFABP Occurs with a Discrete Temperature Increase. Measurement of the activity of binding of IFABP to oleic acid as a function of temperature reveals a bimodal conduct that suggests the occurrence of a concomitant conformational change of the protein. Specifically, in the range of 35−50 °C, this binding activity exhibits a break in the monotonic decreasing behavior with increasing temperature; i.e., the binding activity remains constant (or even increases slightly), an event which we believe can be correlated with a localized structural rearrangement. The direct plot of these data (*B*/*T* vs temperature, Figure 1) depicts this anomalous behavior. In this regard, thermodynamic measurements of the dissociation constant for different fatty acids, including oleate, were derived from fluorescence data using the acrylodan-modified form of IFABP (ADIFAB assay; *23*, *24*). These studies have demonstrated that the binding affinities decrease with increasing temperature in the range of 10−50 °C. However, the increase in binding activity in the range of 35−50 °C could have been overlooked by these authors under the assumption of a linear van't Hoff plot. Alternatively, chemical modification with acrylodan at K27 in ADIFAB (*18*) may influence the mobility of the helical hairpin motif, which is part of the entry portal region, thus preventing this derivative from undergoing such temperature-induced transition. In agreement with this general observed tendency, constants for binding of IFABP to different fatty acids were estimated independently by isothermal titration calorimetry (*35*). However, this last work included data only up to 38 °C. The detection of this anomalous binding phenomenon prompted us to employ spectroscopic techniques to ascertain whether this functional irregularity had a structural correlation.

The Observed Enhancement in Binding Activity Correlates with Spectroscopic Measurements. The near-UV CD spectrum of apo-IFABP reveals a decrease in the magnitude of the most prominent dichroic signal centered at 254 nm in the temperature range of 35−50 °C (panels A and B of Figure 2). Most likely, this observation implies the progressive loss of the chiral environment around phenylalanine residues, some of which are located in the mobile entry portal region (see below). It is noteworthy that the single histidine residue in IFABP (H33), which might also contribute to the near-UV CD spectrum, belongs to this same region. Most significantly, in the presence of oleic acid, this effect is not observed. In fact, significant conservation of this signal occurs up to the highest temperature assayed (65 °C). Although precise measurements in the range of 265−290

Table 3: Most Frequent Dihedral Angles for Conformers of ANS and BisANS Bound to the Cavity of IFABP Encountered during the MD Simulation[a]

	ANS	
	conformer **1b**	conformer **1′b**
dihedral angle (deg)[b]		
Φ_1	6.8 ± 7.0 (19.8 ± 20.0)	−10.7 ± 5.0 (−19.8 ± 17.5)
Φ_2	−105.9 ± 5.0 (−119.3 ± 17.5)	110.2 ± 5.0 (118.4 ± 16.2)
distance (Å)[b]		
$NH_{R106}\cdots OS_8$ hydrogen bond	2.03 ± 0.07	3.10 ± 0.10
$Cz_{F55}-C_{10}$	8.51 ± 0.11	7.96 ± 0.10
$Cz_{F55}-N_1$	11.13 ± 0.11	11.60 ± 0.05
$C\gamma_{D34}-C_{10}$	6.42 ± 0.09	6.80 ± 0.11
$C\gamma_{D34}-N_1$	9.81 ± 0.10	9.44 ± 0.08
$C\alpha_{K27}-C_{10}$	11.83 ± 0.20	11.08 ± 0.05
$C\alpha_{K27}-N_1$	14.31 ± 0.11	14.52 ± 0.05

	BisANS		
	conformer **1b**	conformer **2b**	conformer **3′b**↑
dihedral angle (deg)[b]			
Φ_1	71.0 ± 5.5 (20.2 ± 20.0)	56.9 ± 6.1 (15.2 ± 15.0)	13.2 ± 5.0 (−19.5 ± 17.5)
Φ_2	−141.5 ± 7.8 (−114.1 ± 16.2)	−121.4 ± 4.2 (−109.4 ± 15.0)	65.3 ± 6.3 (119.3 ± 15.0)
Φ_3	110.6 ± 3.9 (−75.0 ± 12.5 and −105.0 ± 12.5)	−48.2 ± 3.0 (−70.0 ± 10.0 and −105.0 ± 10.0)	−45.1 ± 6.3 (−102.5 ± 12.5 and −77.5 ± 12.5)
Φ_4	−130.9 ± 5.0 (−123.5 ± 15.0)	−101.9 ± 4.6 (−116.1 ± 15.0)	−73.9 ± 6.5 (−119.5 ± 17.4)
Φ_5	32.6 ± 5.0 (21.3 ± 21.3)	−11.5 ± 5.4 (17.1 ± 15.0)	−33.8 ± 6.5 (17.6 ± 16.5)
distance (Å)[b]			
$NH_{R106}\cdots OS_8$ hydrogen bond	1.72 ± 0.03	2.00 ± 0.07	2.06 ± 0.10
$Cz_{F55}-C_{9'}$	9.12 ± 0.09	6.71 ± 0.09	6.67 ± 0.08
$Cz_{F55}-N_{1'}$	6.79 ± 0.10	5.88 ± 0.08	5.82 ± 0.10
$C\gamma_{D34}-C_{9'}$	8.30 ± 0.11	5.69 ± 0.09	6.44 ± 0.10
$C\gamma_{D34}-N_{1'}$	8.30 ± 0.12	6.01 ± 0.10	7.52 ± 0.11
$C\alpha_{K27}-C_{9'}$	10.95 ± 0.05	10.13 ± 0.05	9.11 ± 0.07
$C\alpha_{K27}-N_{1'}$	8.15 ± 0.07	8.22 ± 0.07	6.97 ± 0.08

[a] MD simulations at 300 K in vacuo employing the MM2* force field were run for 200 ps. [b] The definition of dihedral angles and distances follows the convention described in the legend of Figure 7A and the footnote of Table 2. The values represent bond angles and distances for the most populated states (mode); the limits for the width of the distribution bell at half-height are reported. The most frequent values of dihedral angles for the corresponding free forms are shown in parentheses. For all angles (except Φ_3 in the free form), no other value was observed to be significantly populated.

nm were hindered by the weak values of ellipticity for signals attributed to tyrosine and tryptophan residues, one can infer that a similar perturbation of the environment around these aromatic residues is concomitantly occurring, as revealed by the generalized flattening observed in this region with increasing temperature. By contrast, no change was observed in the far-UV CD spectrum of apo- or holo-IFABP upon the temperature increasing from 20 to 60 °C; i.e., $[\theta]_M$ at 216 nm remains constant. Only when the denaturation temperature is approached (70 °C) does this signal decrease sharply (data not shown). As this spectral region is dominated by the β-sheet structure, we conclude that secondary structure is well preserved until the protein unfolds, a fact that points to the remarkably high stability of the β-barrel motif. These results are in agreement with earlier reports on the thermal stability of IFABP (*36*).

Independent evidence supporting the stability of the overall structure, in particular, the maintenance of a fixed close-packed structure for the hydrophobic core, comes from measurements of intrinsic fluorescence and fourth-derivative analysis of the UV spectrum.

IFABP contains two tryptophan residues located at different sites (W6 and W82). W82 is buried within the hydrophobic core, and lies at the bottom of the binding pocket close to the carboxylate end of the fatty acid, as known from X-ray crystallography and NMR studies (*9*−*13*). On the other hand, W6 belongs to the first β-strand of the barrel. Both of these residues are nearly occluded from the solvent; the solvent accessible surface area of W6 is null, while that for W82 is only 0.7 Å^2. This last residue contributes to approximately 80% of the intrinsic fluorescence emission of this protein, as evidenced by the analysis of tryptophan mutants (personal communication from I. Ropson, Washington University School of Medicine, St. Louis, MO). Aware of this fact, we took advantage of this fluorophore as a spectroscopic probe of the protein hydrophobic core. In this regard, our experiments indicate (i) the constancy of the center of mass of the intrinsic fluorescence emission spectra of apo- and holo-IFABP as the temperature rises up to the onset of denaturation (Figure 5A) and (ii) the steady decrease of fluorescence intensity (Figure 5B), suggesting that the environment around this residue remains unchanged.

On the other hand, evidence from fourth-derivative UV spectroscopy supports the notion that, on average, the polarity of the milieu around aromatic residues is preserved over a

wide temperature range. The small signal changes observed arise as a consequence of widespread solvent rearrangement around these amino acid residues. Characteristic wavelengths λ_1, λ_2, and λ_4 hardly change, except for a slight drift toward higher values (Figure 4A−C), a phenomenon which is also observed for NATA under the same conditions (Figure 4E,F). In addition, a similar monotonic decrease in the parameter *R* is observed in both cases (Figure 4D,G).

Comparison of the crystallographic (*9*, *10*) and NMR structures (*11*−*13*) of apo- and holo-IFABP indicates that (i) the side chains of residues pointing inward and lining the binding cavity and (ii) those located in the interior close-packed core occupy similar positions in both structures. By contrast, the main conformational differences between these structures occur at the "entry portal" region of IFABP. This region comprises the helix−turn−helix motif, and the neighboring loop connecting β-strands C and D and has been implicated in the access of the ligand to the binding cavity. In the crystal structure, some side chains exhibit discrete disorder in the apo structure, while this is not apparent once the fatty acid is bound. In particular, the conformation of the side chain of F55 appears to play a role as a lid to a channel connecting the bulk solvent with the interior of the cavity. On the other hand, the dynamic picture provided by the NMR structures of apo- and holo-IFABP points to a subregion involving the backbone and side chains of amino acids belonging to the C-terminal half of the second helix (residues 29−36) and the C−D turn (residues 54−57). Five of the eight phenylalanine residues of IFABP are clustered in the hydrophobic core, while F17, F55, and F128 are located in the peripheral region (see Figure 8). When the fatty acid is bound, the accessible surface area of the first two residues decreases by 1.5 and 20.4 Å^2, respectively. By contrast, F128 is completely buried in both apo and holo forms. In view of this analysis, the first two aromatic residues appear to be likely candidates responsible for the changes observed in the near-UV CD spectra. Unlike the situation prevailing in the apo structure, in the holo form, a constraint is imposed on the motion of these side chains due to the interaction with oleic acid.

Structural and Functional Changes Can Be Explained by a Model Involving a Conformational Transition of a Discrete Domain of IFABP. We found ANS and its dimer bisANS to be suitable probes for further testing the dynamic portal hypothesis. The quantum yield of fluorescence of these compounds is greatly enhanced as the polarity of the environment decreases or when spatial restraints, imposed by a rigid binding site, prevent a sufficiently fast relaxation of the excited state (*31*). Under the assumption that these molecules are indeed occupying the binding cavity, this pair could serve as spectroscopic markers for sensing spatially different environments. To this end, we measured the fluorescence emission of each probe when bound to IFABP. Evidence for the location of these molecules within the binding pocket comes from binding experiments which proved that oleic acid was indeed able to displace both fluorescent probes (C. Arighi, J. P. Rossi, and J. M. Delfino, manuscript in preparation; *35*, *37*).

A remarkable difference was observed in the behavior of the complexes between IFABP and each probe (Figure 6). ANS−IFABP experienced a monotonic decay of fluorescence intensity with an increase in temperature, similar to that observed for ANS (or bisANS) dissolved in 1-butanol. On the contrary, bisANS−IFABP showed a deviation from this conduct, which qualitatively resembles the anomalous binding behavior toward oleic acid (Figure 1); a main enhancement of fluorescence intensity occurs in approximately the same temperature range where the conformational transition described before is taking place. One interpretation of this phenomenon results from the added length of bisANS which places the fluorophore very close to the entry portal, therefore, becoming sensitive to changes occurring in this region. To help in the understanding of these results, we modeled tentative structures for these complexes. The main goals of this approach were (i) to establish whether the shape and size of the fluorescent ligands allowed them to be fitted inside the binding cavity and (ii) to describe the environment of the ligand within the cavity so as to evaluate whether predictions derived thereof are compatible with the experimental results.

Modeling of these fluorescent ligands in their bound forms suggests that these probes can be accommodated well within IFABP. For this to happen, some deviations from the optimal values of dihedral angles found for the free forms should occur. This point was shown experimentally in the case of ANS bound to α-chymotrypsin, as determined by X-ray crystallography (*34*). Most importantly, here the binding of this fluorescent ligand to the protein did not bring about any major change in the structure of the enzyme. Nevertheless, the new values of torsional angles still fall within the same allowed energetic regions, due to the shallow shape of the potential energy wells (Tables 1 and 2). In all cases analyzed, molecular dynamics simulations allowed us to conclude that the positioning of the ligand within the binding cavity varies between narrow limits; i.e., interatomic distances and dihedral angles oscillate around the average values reported in Table 3. Not unexpectedly, the confinement of the ligand within the binding cavity was demonstrated to impose a constraint on rotational degrees of freedom.

The angular deviation between the planes of the naphthalene and phenyl rings in ANS is significant (∼67°), a feature that was also observed in the crystal structure of this compound bound to α-chymotrypsin (*34*). In our study, the lowest-energy forms of ANS bound to IFABP differ from each other (**1′b** vs **1b**, Table 2) in the relative orientation of the planes of the aromatic rings; the planes of the naphthalene and phenyl rings in one conformer are almost perpendicular to the corresponding planes in the other. Despite this feature, there is enough space within the cavity to accommodate one conformer or the other. Regardless of orientation, the comparison between these models indicates that a significant overlap occurs between the volume of the bound ligands (63%). Moreover, each moiety of the ligand maps to the same space region within the cavity; i.e., the phenyl and naphthalene rings overlap by 55 and 45%, respectively. In both models, the sulfonate group lies at hydrogen bonding distance from the guanido group of R106 (Table 2), although in model **1′b** the distance between a sulfonate oxygen and a guanido hydrogen falls at the upper limit for such a bond (3 Å; *38*). Nevertheless, in this model the consequent loss in electrostatic energy (17 kJ/mol) is compensated for by better van der Waals contacts (74 kJ/mol). In addition, Q115 could

participate in hydrogen bonding to a second sulfonate oxygen.

The prediction holds that the phenyl moiety of ANS shares a common hydrophobic environment dominated by aromatic residues (W82, F93, Y70, F68, L79, and A104), which could stabilize the complex by π-stacking or edge-to-face interactions (*39*). This phenyl ring is located close to the position occupied by carbon atoms C_5-C_7 of palmitic acid bound to IFABP. In addition, both models predict an interaction between the hydrogen bound to the anilino nitrogen of ANS and the oxygen atom of the side chain of tyrosine residues; namely, these hydrogen bond distances are 2.36 Å for Y70 in model **1b** and 2.54 Å for Y117 in model **1′b**. In both models, residues Y14, Y117, Y70, L36, and L72 make up the environment around the naphthalene moiety. van der Waals contacts in this region account for most of the energy difference, which favors model **1′b** over **1b**; i.e., 1.2 or 4.0%, respectively, of the atomic volume of the ligand overlaps with residues of the cavity. However, the expectation is that minimal movements of the amino acid side chains could relax these tensions. On the other hand, predicted distances between the centroid of the phenyl rings of F55 and that of the phenyl ring of ANS (>13 Å) or C_{10} in the naphthalene moiety (~8 Å) are relatively large to allow an effective interaction of this region of the protein with the fluorophore (Table 2).

In the case of bound bisANS, only three models complied with the selection criteria mentioned above (**1b**, **2b**, and **3′b**↑, Table 2). In these models, one sulfonate group of bisANS is at hydrogen bonding distance from R106, a feature that was maintained during MD runs (Table 3). In conformer **2b**, an additional hydrogen bond is predicted between the imino hydrogen of the indole ring of W82 and an oxygen atom belonging to the proximal sulfonate group of bisANS. All three models predict a unique possible location of the proximal phenyl ring within the binding cavity. This substituent orients itself toward the same hydrophobic pocket where the phenyl ring of bound ANS is located. In conformers **2b** and **3′b**↑, the plane of this ring is parallel to that of F93, where good van der Waals contacts are observed. Unlike bound ANS, the proximal NH in bound bisANS does not seem to participate in hydrogen bonding with neighboring amino acid side chains; however, this does not exclude interactions with water molecules inside the cavity.

The proximal naphthalene moiety of bisANS is in close contact with hydrophobic residues L36, L38, Y70, L72, A73, L78, A104, and Y117. In both conformers **1b** and **2b**, the orientation of the plane of this ring is almost parallel to the phenyl ring of Y70. By contrast, conformer **3′b**↑ has the proximal naphthalene ring parallel to the side chain of Y117. This feature of the models could implicate π-stacking interactions in the stabilization of the bound ligand.

On the other hand, the following residues belong to the environment around the distal naphthalene of bisANS: Y14, F17, S53, L72, A73, L102, and Y117. In conformer **3′b**↑, the hydroxyl group of Y14 points toward this ring. Conversely, conformer **2b** predicts instead a hydrogen bond between the distal amino hydrogen and the hydroxyl oxygen of Y14.

In all models of bisANS, the distal phenyl group shows a preferential location near A73, F55, G31, K27, M18, and I23. It is noteworthy that palmitic acid accommodates its hydrocarbon tail (carbon atoms 14−16, Figure 8B) in the same region of the space. Here, aromatic−aromatic interactions could take place between the distal phenyl ring of bisANS and the side chain of F55, where the different models predict centroid phenyl ring separations between 4.5 and 5.6 Å and dihedral angles between their planes in the range of 58−62° and 90°, well within the limits accepted for this kind of interaction (*39*).

Lowest-energy models **2b** and **3′b**↑ place the distal sulfonate group in a similar position, in close proximity to F55 (a separation of 2.5 Å exists between a distal sulfonate oxygen and a hydrogen bound to C_δ of the phenyl side chain). At variance with the models described above, conformer **1b** places this sulfonate group in the vicinity of F17. In any case, the distal end of bisANS is neighboring the domain of IFABP implicated in the transit of the ligand into the cavity, i.e., the so-called entry portal region.

The possibility that temperature might induce a structural change in bisANS which by itself could be responsible for the anomalous fluorescence enhancement observed (Figure 6) cannot be excluded. Indeed, molecular modeling reveals alternative binding modes for bisANS. It is conceivable that a temperature-induced alteration of the protein environment might favor a particular bound conformer. On the other hand, apart from hydrophobic interactions within the pocket, electrostatic attraction of bisANS to positively charged amino acids localized in the helix−turn−helix lid might also play a role in binding. In this fashion, using molecular modeling we were able to predict that bisANS (unlike ANS) could appropriately probe a putative mobile region of IFABP. Definitive proof of this should come from results from experimentally determined structures of these complexes. In this regard, efforts aimed at their crystallization are currently underway in our laboratory.

Conclusions. IFABP undergoes a conformational transition at low temperatures, which might bear significance for the mechanism of binding of the fatty acid ligand. Results from near-UV CD spectroscopy along with measurements of binding activity support the notion that the small helical hairpin domain, which would act as a flexible lid limiting the entry of the ligand into the cavity, would shift to a form more suitable for ligand binding as the temperature increases. F55 and F17 emerge as possible candidate amino acid residues implicated in this conformational change.

By contrast, results from intrinsic fluorescence measurements, far-UV CD spectroscopy, and fourth-derivative analysis of the UV absorption spectra of IFABP indicate that the major domain involving the β-clam structure would preserve itself intact over this temperature range and only starts to become disorganized at the onset of denaturation. Due to its prominent location within the hydrophobic core of the protein, W82 serves as a suitable probe for this domain.

In addition, results from fluorescence measurements of extrinsic probes interpreted in light of molecular modeling analysis led us to propose that ANS would be sensing a region deep inside the binding cavity, close to R106, whereas the range of bisANS would extend beyond this region, approaching the peripheral helical domain.

Results presented in this paper put special emphasis on the role that the so-called entry portal region plays in the binding activity. In this regard, comparison of the crystal-

lographic structures of holo- and apo-IFABP allowed the authors to propose the movement of the side chain of F55 as the gate through which the fatty acid goes into the cavity (*9*, *10*). A similar role appears to be played by F57 in ALBP (*40*). However, this opening is relatively narrow (about 7 Å wide), and consequently, some additional local rearrangements are expected to occur to facilitate the entry or exit of the fatty acid. Support for this notion came from a MD simulation of the release of palmitic acid from IFABP carried out at different temperatures (*41*). The differential susceptibility to proteolysis on apo and holo cellular retinoid binding proteins provided experimental evidence for a conformational change occurring upon binding of the ligand (*42*). Later on, a study of a helix-less variant of IFABP provided kinetic evidence of a rate-limiting step for the ligand binding reaction implicating the helical domain in a conformational change (*43*). These authors also showed that this domain was not essential for preserving the integrity of the fatty acid binding cavity, but it might instead contribute to regulation of the affinity of the protein for different fatty acids. More recently, the comparison between NMR structures of holo- and apo-IFABP revealed disorder in the apo form in a region involving the C-terminal half of helix II, the linker α-II−*β*-B, and the turns between strands C−D and E−F (*11*−*13*). Our spectroscopic and functional results agree well with the evidence presented above. The added dimension provided by the temperature experiments supports a view whereby the entry portal region should play a dynamic role, which might possibly serve to confer on the protein an important ability to physiologically discriminate among different hydrophobic ligands. To further characterize the binding mechanism, titration and competition experiments involving both fatty acids and fluorescent ligands are currently underway.

ACKNOWLEDGMENT

We dedicate this work to the memory of Dr. Horacio N. Fernández, who inspired the early stages of this study. We thank Dr. Marcelo J. Kogan for his advice on the use of molecular modeling techniques and Dr. Alejandro A. Paladini for his assistance with fluorometric methods.

REFERENCES

1. Glatz, J. F., and van der Vusse, G. J. (1996) *Prog. Lipid Res. 35*, 243−282.
2. Stremmel, W., Strohmeyer, G., Borchard, F., Kochwa, S., and Berk, P. D. (1985a) *Proc. Natl. Acad. Sci. U.S.A. 82*, 4−8.
3. Stremmel, W., Lotz, G., Strohmeyer, G., and Berk, P. D. (1985b) *J. Clin. Invest. 75*, 1068−1076.
4. Jones, T. A., Bergfors, T., Sedzik, J., and Unge, T. (1988) *EMBO J. 7*, 1597−1604.
5. Chytil, F., and Ong, D. E. (1987) *Annu. Rev. Nutr. 7*, 321−335.
6. Pastuszyn, A., Noland, B. J., Bazan, J. F., Fletterick, R. J., and Scallen, T. J. (1987) *J. Biol. Chem. 262*, 13219−13227.
7. Banaszak, L., Winter, N., Xu, Z., Bernlohr, D. A., Cowan, S., and Jones, A. (1994) *Adv. Protein Chem. 45*, 89−151.
8. Sacchettini, J. C., Banaszak, L. J., and Gordon, J. I. (1990) *Mol. Cell. Biochem. 98*, 81−93.
9. Sacchettini, J. C., Gordon, J. I., and Banaszak, L. J. (1989) *J. Mol. Biol. 208*, 327−339.
10. Scapin, G., Young, A. C. M., Kromminga, A., Veerkamp, J. H., Gordon, J. I., and Sacchettini, J. C. (1993) *Mol. Cell. Biochem. 123*, 3−13.
11. Hodsdon, M. E., and Cistola, D. P. (1997) *Biochemistry 36*, 1450−1460.
12. Hodsdon, M. E., and Cistola, D. P. (1997) *Biochemistry 36*, 2278−2290.
13. Hodsdon, M. E., Ponder, J. W., and Cistola, D. P. (1996) *J. Mol. Biol. 264*, 585−602.
14. Daniel, E., and Weber, G. (1966) *Biochemistry 5*, 1893−1900.
15. Cull, M., and McHenry, C. S. (1990) *Methods Enzymol. 182*, 147−153.
16. Lowe, J. B., Sacchettini, J. C., Laposata, M., McQuillan, J. J., and Gordon, J. I. (1987) *J. Biol. Chem. 262*, 5931−5937.
17. Glatz, J. F., and Veerkamp, J. H. (1983) *Anal. Biochem. 132*, 89−95.
18. Richieri, G. V., Ogata, R. T., and Kleinfeld, A. M. (1992) *J. Biol. Chem. 267*, 23495−23501.
19. Lakowicz, J. (1986) in *Principles in Fluorescence Spectroscopy*, pp 43−47, Plenum Press, New York and London.
20. Weber, G. (1992) in *Protein Interactions*, pp 177−198, Chapman & Hall, New York.
21. Mohamadi, F., Richards, N. G. J., Guida, W. C., Liskamp, R., Lipton, M., Caufield, C., Chang, G., Hendrickson, T., and Still, W. C. (1990) *J. Comput. Chem. 11*, 440−467.
22. Chang, G., Guida, W. C., and Still, W. C. (1989) *J. Am. Chem. Soc. 111*, 4379−4386.
23. Richieri, G. V., Ogata, R. T., and Kleinfeld, A. M. (1995) *J. Biol. Chem. 270*, 15076−15084.
24. Richieri, G. V., Ogata, R. T., and Kleinfeld, A. M. (1996) *J. Biol. Chem. 271*, 11291−11300.
25. Bewley, T. A., and Li, C. H. (1972) *Biochemistry 11*, 297−931.
26. Goux, W. J., and Hooker, T. M., Jr. (1980) *J. Am. Chem. Soc. 102*, 7080−7087.
27. Duñach, M., Sabés, M., and Padrós, E. (1983) *Eur. J. Biochem. 134*, 123−128.
28. Padrós, E., Morros, A., Mañosa, J., and Duñach, M. (1982) *Eur. J. Biochem. 127*, 117−122.
29. Sacchettini, J. C., and Gordon, J. I. (1993) *J. Biol. Chem. 268*, 18399−18402.
30. Pace, C. N., Shirley, B. A., and Thomson, J. A. (1989) in *Protein Structure: A Practical Approach* (Creighton, T., Ed.) pp 311−330, IRL Press at Oxford University Press, Oxford, U.K.
31. Slavik, J. (1982) *Biochim. Biophys. Acta 694*, 1−25.
32. Cody, V., and Hazel, J. (1976) *Biochem. Biophys. Res. Commun. 68*, 425−429.
33. Cody, V., and Hazel, J. (1977) *J. Med. Chem. 20*, 12−17.
34. Weber, L. D., Tulinsky, A., Johnson, J. D., and El-Bayoumi, M. A. (1979) *Biochemistry 18*, 1297−1303.
35. Kurian, E., Kirk, W. R., and Prendergast, F. G. (1996) *Biochemistry 35*, 3865−3874.
36. Ropson, I. J., Gordon, J. I., and Frieden, C. (1990) *Biochemistry 29*, 9591−9599.
37. Kirk, W. R., Kurian, E., and Prendergast, F. G. (1996) *Biophys. J. 70*, 69−83.
38. Jeffrey, G. A., and Saenger, W. (1991) in *Hydrogen Bonding in Biological Structures*, pp 15−20, Springer-Verlag, Berlin.
39. Burley, S. K., and Petsko, G. A. (1985) *Science 229*, 23−28.
40. Xu, Z., Bernlohr, D. A., Banaszak, A., Patel, S. B., Veerkamp, J. H., and Sacchettini, J. C. (1994) *Structure 2*, 532−534.
41. Zanotti, G., Feltre, L., and Spadon, P. (1994) *Biochem. J. 301*, 459−463.
42. Jamison, R. S., Newcomer, M. E., and Ong, D. E. (1994) *Biochemistry 33*, 2873−2879.
43. Cistola, D. P., Kim, K., Rogl, H., and Frieden, C. (1996) *Biochemistry 35*, 7559−7565.
44. Kraulis, P. J. (1991) *J. Appl. Crystallogr. 24*, 946−950.

BI981827X